Late onset of the Holocene rainfall maximum in northeastern China inferred from a pollen record from the sediments of Tianchi Crater Lake

Xiaoyan Liu[a], Tao Zhan[b]*, Xinying Zhou[c]*, Haibin Wu[d], Qin Li[d], Chao Zhao[c], Yansong Qiao[e], Shiwei Jiang[a], Luyao Tu[a], Yongfa Ma[b], Jun Zhang[b], Xia Jiang[f], Benjun Lou[b], Xiaolin Zhang[a]*, Xin Zhou[a]*

[a]School of Earth and Space Sciences, University of Science and Technology of China, 230026 Hefei, China
[b]The Second Hydrogeology and Engineering Geology Prospecting Institute of Heilongjiang Province, 150030 Harbin, China
[c]Key Laboratory of Vertebrate Evolution and Human Origins, Institute of Vertebrate Paleontology and Paleoanthropology, Chinese Academy of Sciences, 100044 Beijing, China
[d]Key Laboratory of Cenozoic Geology and Environment, Institute of Geology and Geophysics, Chinese Academy of Sciences, 100029 Beijing, China
[e]Institute of Geomechanics, Chinese Academy of Geological Sciences, 100081 Beijing, China
[f]Heilongjiang Bureau of Geology and Mineral Resources, 150036 Harbin, China
*Corresponding author e-mail address: xinzhou@ustc.edu.cn (Xin Zhou), hljzhantao@163.com (Tao Zhan), Zhouxinying@ivpp.ac.cn (Xinying Zhou) and zhxl2012@ustc.edu.cn (Xiaolin Zhang).

(Received December 8, 2017; Accepted October 18, 2018)

Abstract

The timing of the Holocene summer monsoon maximum (HSMM) in northeastern China has been much debated and more quantitative precipitation records are needed to resolve the issue. In the present study, Holocene precipitation and temperature changes were quantitatively reconstructed from a pollen record from the sediments of Tianchi Crater Lake in northeastern China using a plant functional type-modern analogue technique (PFT-MAT). The reconstructed precipitation record indicates a gradual increase during the early to mid-Holocene and a HSMM at ∼5500–3100 cal yr BP, while the temperature record exhibits a divergent pattern with a marked rise in the early Holocene and a decline thereafter. The trend of reconstructed precipitation is consistent with that from other pollen records in northeastern China, confirming the relatively late occurrence of the HSMM in the region. However, differences in the onset of the HSMM within northeastern China are also evident. No single factor appears to be responsible for the late occurrence of the HSMM in northeastern China, pointing to a potentially complex forcing mechanism of regional rainfall in the East Asian monsoon region. We suggest that further studies are needed to understand the spatiotemporal pattern of the HSMM in the region.

Keywords: Northeastern China; Holocene summer monsoon maximum; Tianchi Crater lake; Pollen-based quantitative reconstruction

INTRODUCTION

The East Asian summer monsoon (EASM) is a major component of the global atmospheric circulation system with significant effects on Earth's energy and hydrological cycles (Dykoski et al., 2005; Peng et al., 2005; Wang et al., 2008). The monsoon climate is critically important for human societies and controls the distribution and dynamics of vegetation in monsoonal Asia (Webster, 2006; Zhou et al., 2007; Cai et al., 2010). Exploring past monsoon system variability,

particularly during the Holocene, is a prerequisite not only for a detailed understanding of global climate processes but also for improving climate prediction (Ran and Feng, 2013; Yu, 2013; Caley et al., 2014; Stebich et al., 2015).

In recent decades, significant advances in our understanding of Holocene monsoon evolution have been made based on numerous studies of lake sediments, cave deposits, peat deposits and aeolian sequences (Wang et al., 2005, 2008; Hong et al., 2005; Dallmeyer et al., 2013; Jin et al., 2014; Xia et al., 2014), but quantitative evaluations are limited. Thus, to better understand the trends and amplitude of Holocene monsoon rainfall variations, more specific proxies and high-resolution quantitative reconstructions are needed.

Most areas of northeastern China are dominated by the East Asian monsoon (EAM). In recent years, with the increasing

number of geological records and model simulations, a dispute has arisen regarding Holocene precipitation trends, especially about the timing of the Holocene summer monsoon maximum (HSMM) in the region. Broadly, two different patterns are evident. Pollen-based records from Bayanchagan Lake (Jiang et al., 2006, 2010) and Qigai Nurr Lake (Sun and Feng, 2013) show an early- to mid-Holocene EASM rainfall maximum from 10,000–6500 cal yr BP and from 9200–4000 cal yr BP, respectively. A quantitative lake-level record from Dali Lake in northeastern China also shows the same pattern (Goldsmith et al., 2017). These records are all consistent with high-resolution and well-dated stalagmite $\delta^{18}O$ records from central-southern China, which broadly follow Northern Hemisphere summer insolation (Wang et al., 2005; Chen et al., 2016). However, other quantitative rainfall records from northeastern China exhibit a mid- to late-Holocene EASM maximum. The reconstructed mean annual precipitation (P_{ann}) records from the sediments of both Daihai Lake (Xu et al., 2010) and Dali Lake (Xiao et al., 2015) indicate that the HSMM did not occur before 8000 cal yr BP; however, reconstructed precipitation at Sihailongwan Lake increased continuously until approximately 4000 cal yr BP (Stebich et al., 2015). Such striking discrepancies, together with the paucity of high-resolution reconstructions for the region, hinder our understanding of the timing and forcing mechanisms of the HSMM. Thus, new quantitative records from northeastern China are essential.

Here we present fossil pollen spectra and pollen-based quantitative reconstructions of temperature and precipitation for the past 10,300 years derived from the sediments of Tianchi Crater Lake in northeastern China. We then compare our results with other paleoclimate records to assess the timing of the HSMM in the region and to gain improved insights into the possible forcing mechanisms.

MATERIALS AND METHODS

Regional setting and sampling

Nangelaqiu Hill (126°E, 48°44′N) is a 149.9-m-high volcano with an elevation of 596.9 m located in the Wudalianchi Global Geopark, Heilongjiang Province, China. The volcano erupted at ~0.8 Ma (Gong, 1997) and ~0.46 Ma (Liu, 1987). Tianchi Crater Lake (Fig. 1), at the summit of Nangelaqiu Hill, is a typical crater lake with a diameter of ~250 m. The lake was used for irrigation in the 1970s and consequently today is swampy, with abundant growth of aquatic plants. The modern vegetation around Tianchi Crater Lake is categorized as temperate mixed conifer-broad-leaved forest dominated by *Betula platyphylla*, *Populus davidiana*, *Larix gmelinii*, *Corylus* and *Quercus mongolica*; typical herbs include *Artemisia annua* and Chenopodiaceae (Shen et al., 2011; Zhao, 2015).

The area experiences a typical cold temperate monsoon climatic regime with long cold winters and short cool summers. The annual average air temperature is 0–0.5 °C and the average precipitation is ~470 mm, falling mainly during June to August; the mean annual evaporation of the region is ~1260 mm. The ratio of the catchment area to lake area is about 2.8. There are no inflows or outflows and therefore the sediments of Tianchi Crater Lake are well suited for studying the evolution of the EAM.

Two sediment cores, TC1 and TC2, were collected from Tianchi Crater Lake in October 2011 and November 2012,
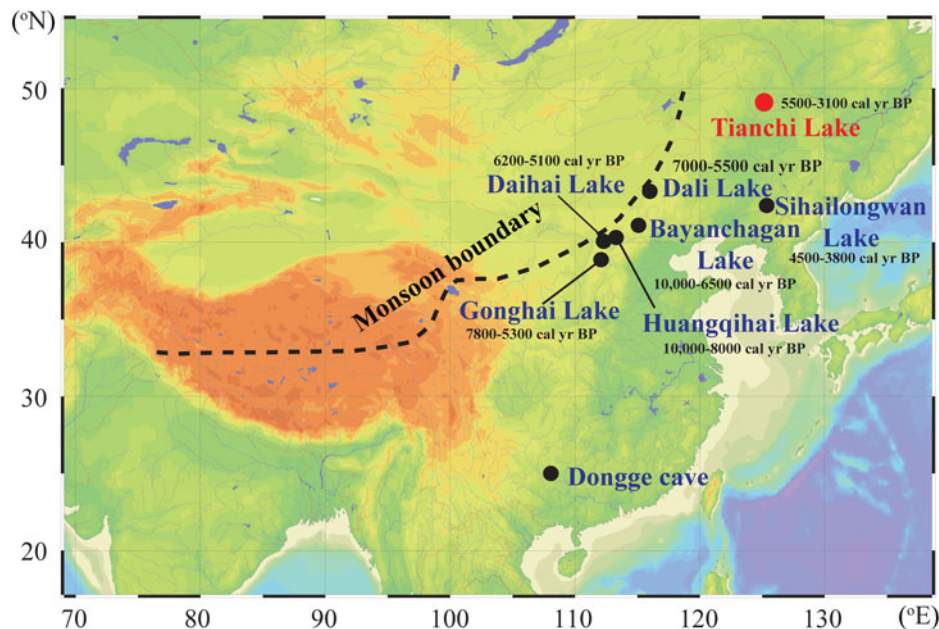

Figure 1. Location of Tianchi Crater Lake (The base map was produced using Ocean Data View software). The black dashed line indicates the modern monsoon boundary (Chen et al., 2018; An et al., 2000). The red dot shows the study site and the black dots are sites mentioned in the text. (For interpretation of the references to color in this figure legend, the reader is referred to the web version of this article.)

respectively, using a 55-mm-diameter percussion corer. Core TC1 was 309 cm in length, compressed to 197 cm in length. Core TC2 was 500-cm long and only the upper 306 cm was used in this study.

Dating method, *n*-alkane analysis and pollen analysis

Sixteen accelerator mass spectrometry (AMS) ^{14}C dates of bulk sedimentary organic matter, leaves, and seeds from core TC1 were obtained at the University of Georgia and the University of Ottawa (Table 1). The results were calibrated to calendar ages using the IntCal13 calibration curve (Reimer et al., 2013). The organic content of 764 samples was measured by weight loss-on-ignition (LOI). Samples from core TC1 were measured at approximately 0.5-cm intervals, and those from core TC2 were measured at 0.5-cm and 1-cm intervals above and below 103 cm, respectively. The samples were homogenized using a mortar and pestle and passed through a 120-μm sieve. Samples weighing 0.5–1.0 g were heated to 105°C for 12 h to constant weight and then combusted at 550°C for approximately 2 h to constant weight, from which $LOI_{550°C}$ was calculated. The analytical error is <1%.

Thirty-seven sediment samples were freeze-dried and finely ground with an agate mortar for *n*-alkane analysis. Approximately 2 g of each sample were extracted with dichloromethane for three cycles of 10 minutes each, using an Accelerated Solvent Extractor (Dionex ASE 350). The extracted total lipids were further separated through silica gel chromatography. The *n*-alkane fraction, eluted with 4 ml *n*-hexane, was analyzed on an Agilent 7890 Gas Chromatography (GC), equipped with a flame ionization detector, at the University of Hong Kong. The *n*-alkanes were identified and quantified by comparing with the retention time of known

n-alkane standards and the external standard of C_{36} *n*-alkane, respectively (Liu et al., 2014). More details of sample preparation and lipid analysis can be found in Sun et al. (2012). The *n*-alkane-based proxy P_{aq} was used to assess the inputs of submerged/floating macrophytes relative to those from emergent aquatic and terrestrial plants. Calculation of P_{aq} was based on the relative proportion of mid-chain (C_{23}, C_{25}) to long-chain (C_{29}, C_{31}) *n*-alkane homologues ($P_{aq} = (C_{23} + C_{25})/(C_{23} + C_{25} + C_{29} + C_{31})$) (Ficken et al., 2000).

A total of 48 pollen samples from core TC2 were obtained at 5-cm intervals. The samples were processed using heavy liquid separation (Moore and Webb, 1978) and acetolysis (Erdtman, 1960). *Lycopodium* tablets were added to the samples to calculate pollen concentrations (Peck, 1974). At least 300 pollen grains were counted for each sample.

The plant functional type-modern analogue technique (PFT-MAT) (Peyron et al., 1998) was applied to the fossil pollen data to quantitatively reconstruct annual precipitation and temperature. This method produces the best results among other quantitative methods applied in northern China, including the MAT, pollen response surface (PRS), and transfer function (TF) approaches (Jiang et al., 2006; Sun and Feng, 2013;). In the procedure, fossil pollen data were assigned to PFTs and then compared with PFTs derived from modern pollen data (Table 2), with the climatic parameters of the best modern analogues used to provide climate values for the fossil pollen spectra via an artificial neural network technique (Peyron et al., 1998). For biome reconstruction, the PFTs were classified into vegetation biomes based on the known ecology and biogeography of modern plants (Table 3) (Prentice et al., 1996). In this study, both the quantitative reconstruction and biome reconstruction were accomplished based on a modern pollen dataset featuring 211 surface pollen spectra from north China (Tables 2 and 3) (Members of China Quaternary Pollen Data Base, 2000, 2001).

Table 1. Radiocarbon dates for core TC1.

Lab Code	Material	Depth (cm)	[14]C age (yr BP)	$\delta^{13}C$ (‰)	Calibrated age (cal yr BP, 2σ)
10110	Organic matter	16	200 ± 25	−27.3	144–215
13190	Seeds	24.5	730 ± 25	−27.6	655–701
13193	Seeds	29	1560 ± 30	−25.4	1387–1529
10111	Organic matter	41.5	2740 ± 30	−27.19	2765–2885
UOC-1162[a]	Leaves	52	3671 ± 37	[b]	3894–4092
13191	Leaves	65	4190 ± 30	−24.9	4622–4764
13192	Leaves	83	5580 ± 35	−24.2	6297–6414
UOC-1163[a]	Leaves	90.5	6083 ± 51	[b]	6796–7031
10112	Organic matter	101	6350 ± 30	−26.57	7240–7331
10114	Organic matter	120	7170 ± 30	−26.14	7943–8024
10113	Organic matter	147	8130 ± 30	−25.03	8999–9133
10115	Organic matter	161	8810 ± 30	−24.58	9694–9938
13194	Seeds	177	9080 ± 30	−26	10,197–10,258
13195	Seeds	184	11,180 ± 35	−20.8	12,989–13,115
10116	Organic matter	197	11,860 ± 30	−26.65	13,575–13,758
13196	Leaves	197	10,660 ± 35	−24.8	12,566–12,702

[a]Measured at the University of Ottawa; all other dates were measured at the University of Georgia.
[b]Not provided by the laboratory.

Table 2. Plant functional types and the corresponding assigned major pollen taxa (Members of China Quaternary Pollen Data Base, 2001)

Code	Plant functional type	Main pollen taxa included
aa	Artic-alpine swarf shrub	*Betula*, Betulaceae, Cupressaceae, *Salix*
af	Artic/alpine forb	Campanulaceae, *Caragana*, Caryophyllaceae, Asteraceae, Brassicaceae, *Polygonum*
bec	Boreal evergreen conifer	*Abies*, *Picea*, *Pinus* (Haploxylon)
bs	Boreal summergreen	*Alnus*, *Betula*, *Populus*, *Salix*
bs1	Cool boreal summergreen	*Betula dahurica*, *B. ermanii*, *B.fruticosa*, *B.ovalifolia*
bsc	Boreal summergreen conifer	*Larix*
bts	Boreal-temperate summergreen shrub	*Lonicera*
ctc	Cool-temperate confer	*Abies*, Taxaceae, *Taxus*, *Tsuga*
df	Desert forb/shrub	*Artemisia, Calligonum, Caragana*, Caryophyllaceae, Chenopodiaceae, Asteraceae, Brassicaceae, Elaeagnaceae, *Elaeagnus*, *Ephedra*, Leguminosae, Liliaceae, *Nitraria*, *Polygonum, Potentilla*
ec	Eurythermic conifer	Cupressaceae, *Juniperus*, Pinaceae, *Pinus* (Diploxylon)
g	Grass	Gramineae, *Hierochloe*, Poaceae
h	Heath	*Empetrum*, Ericaceae, *Vaccinium*
s	Sedge	*Carex*, Cyperaceae, *Cyperus*
sf	Shrub	*Artemisia*, *Aster*, *Astragalus*, Campanulaceae, Capparidaceae, *Caragana*, Caryophyllaceae, Chenopodiaceae, Asteraceae, Brassicaceae, *Daphne*, *Dianthus*, Elaeagnaceae, *Elaeagnus*, *Filifoli-um*, Polygonaceae, *Polygonum*, *Potentilla*, *Primula*, Primulaceae, Ranunculaceae
te	Tropical evergreen	*Altingia*, Anacardiaceae, Annonaceae, Apocynaceae, Araliaceae, *Calamus*, *Canarium*, Combre-taceae, *Cycas*, *Elaeocarpus*, *Ficus*, Flacourtiaceae, Hamamelidaceae, *Helicia*, *Macaranga*, Melastomataceae, Meliaceae, Moraceae, Myristicaceae, Myrtaceae
tef	Tropical evergreen forb	*Acalypha,* Amaranthaceae, Araceae, *Aralia*,Campanulaceae, *Cannabis*, Gesneriaceae, *Impatiens*, Liliaceae, *Lilium*, Lythraceae, *Phyllanthus*, *Pyrola*, *Rhynchodia*, *Ricinus*, *Sageretia*, *Saururus*, *Stephania*, *Ventilago*, Verbenaceae, *Vicia*, *Vittaria*
tf	Temperate forb	*Aconitum*, *Allium*, *Alternanthera*, Amaryllidaceae, *Arabis*, Araceae, *Arachis*, *Arctium*, Boraginaceae, *Caulophyllum*, *Corydalis*, Cucurbitaceae, *Cuscuta*, *Deutzia*, *Euphorbia*, Euphorbiaceae, *Galium*, Geraniaceae, *Glycine*, *Humulus*, *Hypecoum*, Lardizabalaceae, Leguminosae, *Leonurus*, *Lycium*, *Lysimachia*, Onagraceae, *Origanum, Orobanche*, *Orostachys*, Papaveraceae, Papilionaceae, *Paraphlomis*, *Phlomis*, *Platycodon*, Polemoniaceae, *Polygala*, *Pyrola*, *Rheum*, *Rubia*, Solanaceae
tr	Tropical raingreen	*Aeschynanthus*, *Allomorphia*, *Anodendron*, *Aphanamixis*, Bombacaceae, *Bombax*, *Caesalpinia*, Combretaceae, *Decaspermum*, *Elytranthe*, Euphorbiaceae, *Ficus*, *Flacourtia*, *Hainania*, *Microtropis*, *Nyssa*, Olacaceae, Sapotaceae, Syzygium, *Terminalia*, Flacourtiaceae, *Pistacia*, *Acacia*, *Sapium*, *Lithocarpus*
ts	Temperate summergreen	*Acer*, *Aralia*, Araliaceae, *Berberis*, Betulaceae, Celastraceae, *Clematis*, Cornaceae, *Cornus*, *Cotoneaster*, *Crataegus*, *Evodia*, *Fraxinus*, *Hypericum*, *Jasminum*, Myrsinaceae, Oleaceae, *Osmanthus*, *Platanus*, *Quercus*-(*deciduous*), *Rhamnus*, *Rhus*, Rosaceae, Rubiaceae, Rutaceae, *Salix*, *Sambucus*, *Spiraea*, *Tilia*, *Toxicodendron*, *Vaccinium*, *Viburnum*, *Vitex*
ts1	Cool-temperate summergreen	*Alnus*, *Carpinus*, *Corylus*, *Ostryopsis*, *Sorbus*, Ulmaceae, *Ulmus*
ts2	Warm-temperate summergreen	*Ailanthus*, *Albizia*, *Alnus*, *Broussonetia*, Caprifoliaceae, *Carpinus*, *Carya*, *Celtis*, *Cyclocarya*, *Diospyros*, Ebenaceae, *Elaeagnus*, *Fagus*, *Fontanesia*, *Forsythia*, *Ginkgo*, Hamamelidaceae, *Juglans Lagerstroemia*, *Liquidambar*, *Liriodendron*, *Melia*
ts3	Southern warm-temperate summergreen	*Albizia*, *Corylopsis*, Ebenaceae, *Fontanesia*, *Helwingia*, *Liriodendron*, *Rhus*, *Sapium*, *Zelkova*
tsc3	Southern warm-temperate conifer	*Pseudolarix*, Taxodiaceae, *Taxodium*
tx	Tundra	*Cyathea*, Cyatheaceae, Davalliaceae
wtc	Warm-temperate evergreen conifer	*Cedrus*, *Cryptomeria*, *Cunninghamia*, *Dacrydium*, *Glyptostrobus*, *Keteleeria*, *Podocarpus*, Taxaceae, *Taxus*, *Tsuga*
wte	Warm-temperate broad-leaved evergreen	*Acalypha*, *Actinidia*, *Alangium*, *Alchornea*, *Aleurites*, *Allophylus*, Anacardiaceae, *Aralia*, Araliaceae, Bignoniaceae, *Camellia*, *Castanopsis*, Celastraceae, *Cyclobalanopsis*, *Distylium*, *Dodonaea*, *Elaeocarpus, Engelhardtia*, Euphorbiaceae, *Eurya*, *Excoecaria*, *Ficus*, Flacourtiaceae, Hamamelidaceae, *Hamamelis*, *Lithocarpus*, Loranthaceae, *Macaranga*, *Maesa*, *Mallotus*, Meliaceae, Menispermaceae, Moraceae, Myrsinaceae, Myrtaceae, Oleaceae, *Phoebe*, Pittosporaceae, Proteaceae, *Quercus*-(evergreen), *Reevesia*, Rubiaceae, Rutaceae, Sapindaceae, *Schefflera*, *Schima*, *Sycopsis*
wte1	Cool-temperate broad-leaved evergreen	*Hedera*, *Ilex*, *Ligustrum*, Loranthaceae, *Rhododendron*
wte2	Warm temperate sclerophyllous shrub	Capparidaceae, *Capparis*, *Dodonaea*, Ericaceae, Nyctaginaceae, *Olea*, Oleaceae, Proteaceae, *Quercus*-(evergreen), *Zanthoxyllum*

Table 3. Biome definitions in terms of plant functional type. (Members of China Quaternary Pollen Data Base, 2001)

Biome name	Code	Plant functional types
Tropical rainforest	TRFO	te+ wtc+ wte+ tx
Tropical seasonal forest	TSFO	te+ tr+ wtc+ wte+ tx
Tropical dry forest/ savanna	TDFO	tr+ tg
Cold deciduous forest	CLDE	bs+ bsc+ ec+ h+ bs1
Taiga	TAIG	bs+ bsc+ bec+ ec+ h+ bs1+ bts
Cold mixed forest	CLMX	bs+ bsc+ ctc+ ts1+ ec+ h+ bs1 + bts
Cool conifer forest	COCO	bs+ bec+ ctc+ ec+ h+ bs1+ bts
Temperate deciduous forest	TEDE	bs+ ctc+ ts+ ts1+ ts2+ wte1+ ec+ h+ bts
Cool mixed forest	COMX	bs+ bec+ ctc+ ts+ ts1+ ec+ h+ bs1+ bts
Warm mixed forest	WAMF	ts+ ts2+ ts3+ tsc3+ wte+ wtc+ wte1+ ec+ h+ tx+ bts
Xerophytic woods/ scrub	XERO	wte+ wte2+ ec
Tundra	TUND	aa+ g+ s+ af+ ax+ h
Steppe	STEP	sf+ g
Desert	DESE	df

See Table 2 for plant functional types.

RESULTS AND DISCUSSION

Chronology and lithology

The 16 AMS ^{14}C dates from core TC1 are in stratigraphic order, with the exception of the bottom of the core, where two samples from 197 cm have different ages: 12,600 cal yr BP for leaves and 13,700 cal yr BP for bulk sediment
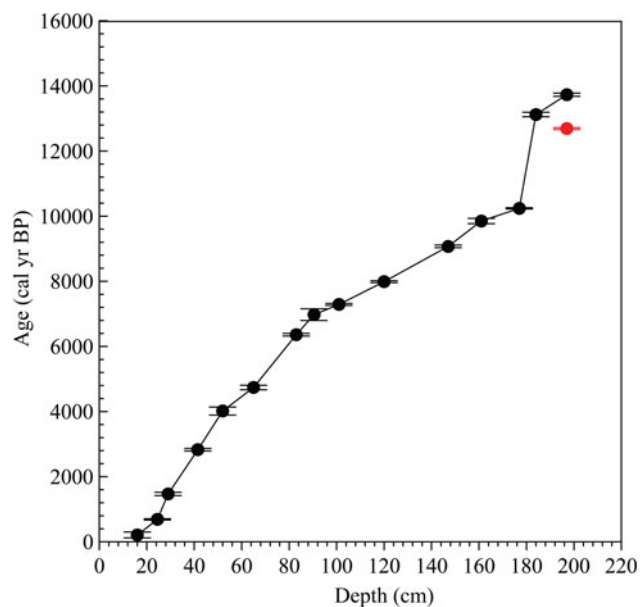

Figure 2. Age-depth relationship for core TC1. The red dot represents a date that was excluded in the construction of an age-depth model. (For interpretation of the references to color in this figure legend, the reader is referred to the web version of this article.)

(Table 1, Fig. 2). The date for the leaves is out of stratigraphic order, and it is possible that this is the result of downward movement of material during coring. Thus, the bulk sediment sample was used in the age-depth model. The chronology of core TC2 was obtained by correlating its $LOI_{550°C}$ record with that of TC1 (Fig. 3). For core TC2, the calculated sedimentation rates for the depth intervals 0–145.5 cm, 145.5–239 cm, and 239–cm to the base are 0.02 cm yr^{-1}, 0.03 cm yr^{-1} and 0.01 cm yr^{-1}, respectively.

The upper 125 cm of core TC1 is greyish yellow in color with substantial organic residues; the interval below 125 cm is black, and that below 187 cm contains numerous red particles of volcanic material that are <2 mm in diameter (Fig. 3). The lithology of core TC2 is similar to that of core TC1. Although the $LOI_{550°C}$ values of the sediments are high, reaching ∼80% at 50–70 cm in core TC1 (Fig. 3), the sediments are classified as lake sediments based on the P_{aq} record. P_{aq} values in sediments of core TC1 are generally higher than 0.4 (Fig. 3), suggesting important inputs from submerged/floating plants to the sedimentary organic matter (Ficken et al., 2000; Xu and Jaffé, 2009).

Pollen evidence for changes in vegetation and climate

The pollen assemblage of the surface sediment layer is characterized by high percentages of *Betula*, *Larix*, *Corylus,* and *Quercus*, reflecting the temperate mixed conifer-broad-leaved forest present in the study area today (Fig. 4). Five pollen assemblage zones were defined by stratigraphically constrained cluster analysis (CONISS) (Grimm, 1987) of the major pollen taxa (Fig. 4).

Zone I (10,300–6900 cal yr BP): This zone is characterized by high percentages of herb pollen (51%–69%, average of 62%, the same below, with the parenthetical percentages referring to a range and an average for Zone I and Zone III), most of which is *Artemisia* (24%–40%, 31%), Liliaceae (0%–14%, 5.2%), Poaceae (1%–9%, 4.5%), *Tamarix* (2%–11%, 4.4%), Asteraceae (2%–7%, 4.0%), Chenopodiaceae (2%–5%, 3.1%) and *Thalictrum* (1%–5%, 2.8%). The individual percentages of *Ephedra*, Brassicaceae, Apiaceae, *Plantago*, Rosaceae, and other herbs are <1% on average. The total percentages of broad-leaved trees (mainly *Betula*, *Ulmus*, *Salix* and *Carpinus*) are ∼25%–46% (Fig. 4), and thus sparse forest steppe-vegetation type is indicated in this zone (Table 4). During this period, herbs were dominant and the pollen percentages of typical drought-tolerant herbs (*Artemisia* and Chenopodiaceae) are well represented, indicating a relatively dry climate (Fig. 4); in addition, the relatively high pollen percentages of thermophilic plants (e.g., *Ulmus japonica*) suggest a relatively warm climate. The higher desert (DESE) and steppe (STEP) biome scores and lower cool conifer forest (COCO) and taiga (TAIG) biome scores (Fig. 5) also confirm the occurrence of a warm and dry climate.

Zone II (6900–5500 cal yr BP): The pollen percentages of herbaceous taxa (*Artemisia*, Poaceae, and *Ephedra*)

Figure 3. (color online) Lithology and correlation of the LOI$_{550°C}$ records of cores TC1 and TC2 (P$_{aq}$ values: unpublished data. The values of P$_{aq}$ are generally higher than 0.4, suggesting typical lake condition).

decreased considerably in this zone, whereas those of broad-leaved trees (*Quercus*, *Betula*, *Salix,* and *Corylus*) increased steadily; in addition, the pollen percentages of *Ulmus* decreased slightly (Fig. 4). These characteristics, in accord with the decreasing DESE and STEP biome scores and the increasing COCO and TAIG biome scores (Fig. 5), indicate that the vegetation type was typical forest steppe (Table 4) and that the climate had become cooler and wetter.

Zone III (5500–3100 cal yr BP): This zone is characterized by high tree pollen percentages (50%–70%, 62%), most of which are broad-leaved trees (42%–62%, 56%), including *Betula* (21%–39%, 29%), *Quercus* (7%–23%, 12%), and *Corylus* (2%–9%, 6%). The pollen percentages of broad-

leaved trees pollen reached a maximum in the zone (Fig. 4). We infer that Tianchi Crater Lake area was occupied by *Quercus*- and *Betula*-dominated deciduous broad-leaved forest vegetation during this period (Table 4). During the mid-Holocene (5500–3100 cal yr BP), the pollen percentages of broad-leaved trees, especially *Quercus*, *Betula,* and *Corylus*, increased substantially and reached a maximum, while pollen percentages of the drought-tolerant herbs (e.g., *Artemisia* and Chenopodiaceae) decreased. A previous study showed that *Quercus mongolica* was an important component of the forest in northeastern China during the Holocene (Ren and Zhang, 1998). At present, *Quercus mongolica* forest is generally distributed in regions of northeastern China with an annual

Figure 4. Pollen percentage diagram for Tianchi Crater Lake.

Table 4. Summary of the vegetation history of Tianchi Crater Lake.

Age (cal yr BP)	Vegetation type	Major pollen indicator taxa	Climatic conditions
10,300–6900	Sparse forest steppe	*Larix, Betula, Ulmus, Quercus, Artemisia,* Liliaceae	Warm and dry
6900–5500	Forest steppe	*Betula, Quercus, Salix, Artemisia*	Cool and wet
5500–3100	*Betula-* and *Quercus-*dominated deciduous broad-leaved forest	*Quercus, Betula, Corylus*	Cold and wettest
3100–800	Forest steppe with increased canopy density	*Quercus, Betula, Artemisia*	Cold and dry
800–0	Sparse forest steppe	*Quercus, Betula, Artemisia,* Poaceae	Cold and dry

average temperature of 3–6°C and annual average precipitation of 600–757 mm (Xia, 1988). Therefore, we infer that this interval corresponds to the Holocene rainfall maximum, with the highest Holocene lake level.

Zone IV (3100–800 cal yr BP): The pollen percentages of trees and broad-leaved trees decreased to average values of 54% and 47%, respectively, and reached their minima at ~2300 cal yr BP, which are lower than in both Zone III and Zone II. Forest steppe with increasing canopy density is suggested by the high percentage of broad-leaved tree pollen (Table 4). In this zone, the decreasing pollen percentages of broad-leaved trees (e.g., *Corylus* and *Carpinus*) and the increasing herb-pollen percentages, including *Artemisia*, Chenopodiaceae, and *Tamarix* (Fig. 4), suggest the occurrence of a relatively dry climate, which is confirmed by the decreasing temperate deciduous forest (TEDE) and cool mixed forest (COMX) biome scores (Fig. 5).

Zone V (800 cal yr BP to present): Herb-pollen percentages show a sustained increase to an average of 52%, reaching a peak of ~60% at 230 cal yr BP. In particular, Poaceae percentages increase substantially after ~300 cal yr BP. After ~800 cal yr BP, tree pollen percentages decreased substantially, but those of some cold-resistant taxa, such as *Picea*, increased at ~400–200 cal yr BP, indicating a cold climate, which is temporally correlated with the Little Ice Age (Mann et al., 2008). During this period, typical sparse forest steppe was dominant in the Tianchi Crater Lake area (Table 4). Notably, the abrupt increase in Poaceae after ~300 cal yr BP may indicate intensive human activity (Tarasov et al., 2006; Zhao et al., 2009), which is confirmed by the onset of widespread dune remobilization in the deserts of northeastern China (Guo et al., 2018). Furthermore, archaeological sites dating to the late Holocene are uncommon in this region (Li, 2016), suggesting that human
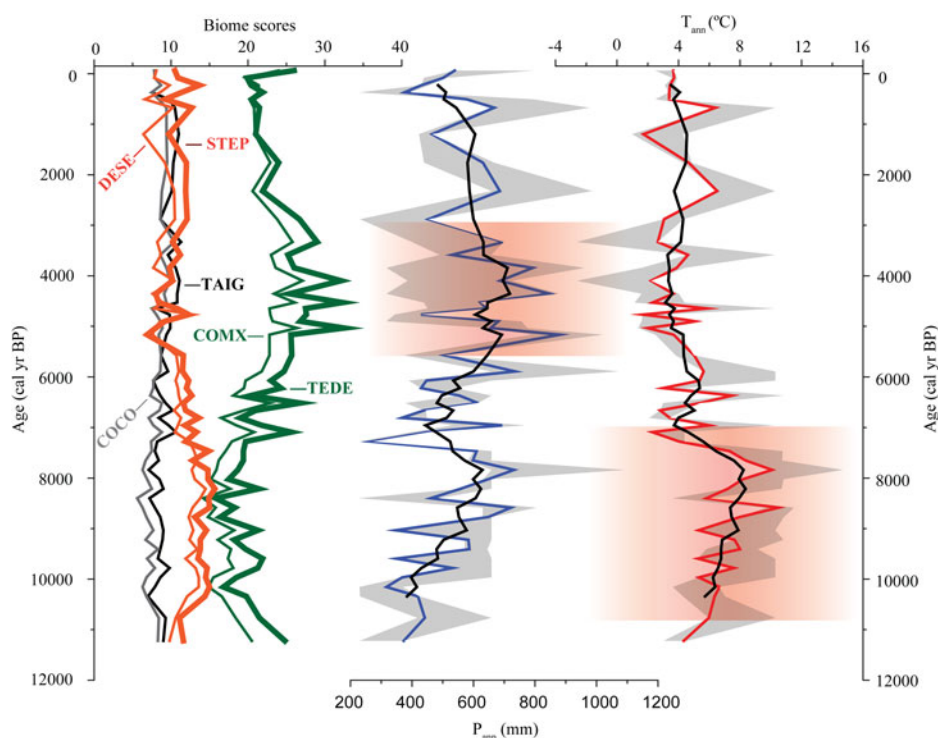

Figure 5. (color online) PFT-MAT-based reconstructed annual precipitation (P_{ann}), annual temperature (T_{ann}) and biome scores for Tianchi Crater Lake. The black smoothed curves are five point running averages; the grey shaded bands indicate the level of uncertainty; and the pink shading indicate Holocene temperature and precipitation maxima.
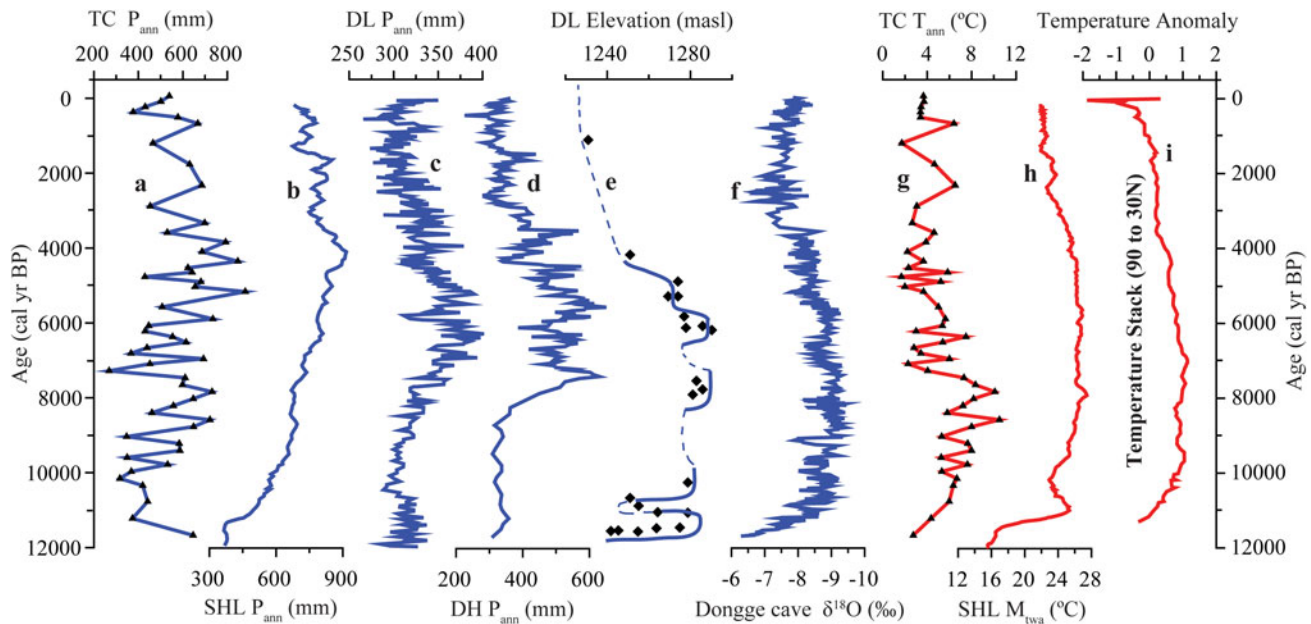
Figure 6. (color online) Comparison of regional climate records from northeastern China, southern China and high latitudes of the Northern Hemisphere. (**a**) Reconstructed P_{ann} record from Tianchi Crater Lake; (**b**) Reconstructed P_{ann} record from Sihailongwan Lake (Stebich et al., 2015); (**c**) Reconstructed P_{ann} record from Dali Lake (Xiao et al., 2015); (**d**) Reconstructed P_{ann} record from Daihai Lake (Xu et al., 2010); (**e**) Lake-level record from Dali Lake (Goldsmith et al., 2017); (**f**) $\delta^{18}O$ record from Dongge cave (Dykoski et al., 2005); (**g**) Reconstructed T_{ann} record from Tianchi Crater Lake; (**h**) Reconstructed mean temperature of the warmest month (M_{twa}) from Sihailongwan Lake (Stebich et al., 2015); (**i**) Temperature anomaly record for high latitudes of the Northern Hemisphere (Marcott et al., 2013).

disturbance was low for most of the Holocene but was higher after ~300 cal yr BP.

Quantitative climate reconstructions

The PFT-MAT-based reconstructed P_{ann} record for Tianchi Crater Lake has a similar trend of variation to that of the pollen percentage diagram (Fig. 5). The ranges of P_{ann} and T_{ann} are 268–881 mm and 1.7–10.5°C, respectively. P_{ann} increased gradually during the early Holocene and then increased abruptly at ~6500 cal yr BP, with the most humid phase from ~5500–~3100 cal yr BP. In accord with the interpretation of the changes in the pollen spectra, the P_{ann} record clearly indicates that the wettest climate occurred during the mid- to late Holocene (Fig. 5) when annual precipitation exceeded 600 mm. However, variations in T_{ann} exhibit a different pattern with a marked rise from the beginning of the early Holocene and a peak at 9000–8000 cal yr BP.

The trend of the PFT-MAT-based reconstruction of T_{ann} for Tianchi Crater Lake is consistent with that of other temperature records from northeastern China and with a temperature anomaly record for high latitudes of the Northern Hemisphere (Fig. 6). This suggests the similar forcing of Holocene temperature changes, probably due to changes in Northern Hemisphere summer insolation (Laskar et al., 2004; Wen et al., 2010). The above-mentioned decoupling of precipitation and temperature has been observed in other paleoclimatic studies (Peterse et al., 2011; Nie et al., 2013) and was attributed to various mechanisms, including latent

heat export from the Southern Hemisphere Indian Ocean (Clemens and Prell, 2007), glacial boundary conditions (Liu et al., 2006), and cold temperature anomalies reconstructed from North Atlantic sediments (Cheng et al., 2009).

Holocene monsoonal precipitation changes in northeastern China

The P_{ann} records from Daihai Lake (Xu et al., 2010), Sihailongwan Lake (Stebich et al., 2015), and Dali Lake (Xiao et al., 2015) all show a mid-Holocene rainfall maximum, which is also confirmed by the record of effective precipitation from the Hani peatland reconstructed from biomarker lipid composition (Zhou et al., 2010). A pollen record from Gonghai Lake, in the adjacent region, reveals a monsoon precipitation maximum from 7800–5300 cal yr BP (Chen et al., 2015), which was confirmed by a long-chain n-alkanes $\delta^{13}C$ record (Rao et al., 2016) and is a little earlier than records from northeastern China. In general, the reconstructed monsoon precipitation maxima in northeastern China are temporally consistent, with slight differences between the onset times.

However, the mid-Holocene rainfall maximum recorded from Tianchi Crater Lake in the above-mentioned records is much later compared with that recorded from Bayanchagan Lake (Jiang et al., 2010) and with the lake-level highstands at Dali Lake (Goldsmith et al., 2017) and Huangqihai Lake (Zhang et al., 2016). The earlier maxima may be unreliable due to differences in methods and to the influence of
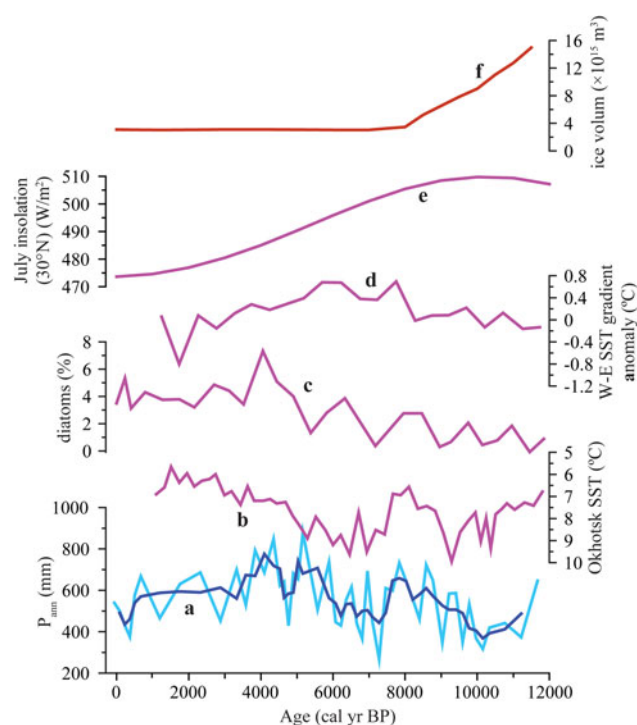
Figure 7. Comparison of the pollen-derived quantitative precipitation record (P_{ann}) for Tianchi Crater Lake with other paleoclimatic records; (**a**) Reconstructed P_{ann} from Tianchi Crater Lake (light blue curve) and the five points running average (dark blue curve); (**b**) Okhotsk SST (Max et al., 2012); (**c**) Relative abundance of sea-ice-related diatoms from the western Okhotsk Sea (Harada et al., 2014); (**d**) East-west SST gradient anomalies in the equatorial Pacific (Koutavas and Joanides, 2012); (**e**) North Hemisphere summer (July) insolation at 30°N (Laskar et al., 2004); (**f**) Northern Hemisphere ice volume (Peltier et al., 2004). (For interpretation of the references to color in this figure legend, the reader is referred to the web version of this article.)

hydrological factors other than monsoon precipitation. The pollen-based P_{ann} record from Bayanchagan Lake (Jiang et al., 2010) contains an early- to mid-Holocene monsoon precipitation maximum, which may be attributed to differences between the numerical reconstruction methods (Jiang et al., 2006, 2010). The early-Holocene lake-level highstand at Huangqihai Lake was thought to be controlled by other factors in addition to monsoon precipitation (Zhang et al., 2016). The lake-level record for Dali Lake may also have been controlled by other factors (Liu et al., 2017; Wen et al., 2017), including runoff from snow/ice melting in the Da Hinggan Range (Xiao et al., 2008; Liu et al., 2017), the underground water supply, and underestimation of the drainage area of Dali Lake (Wen et al., 2017).

Causal mechanisms of Holocene monsoon precipitation in northeastern China

Low-latitude summer insolation changes are generally considered to be the main external forcing mechanism of changes in monsoon precipitation (Dykoski et al., 2005; Chen et al.,

2008). However, the trend of Holocene monsoon precipitation records in northeastern China differs from that of low-latitude Northern Hemisphere summer insolation (Fig. 7), suggesting that internal forcing factors within the Earth system were also important. Such internal factors include shrinkage of the Northern Hemisphere ice sheets (Wen et al., 2010; Chen et al., 2015) and related sea-level variations (Li et al., 2014; Wen et al., 2017), changes in the east-west thermal gradient in the equatorial Pacific (Rao et al., 2016), sea surface temperature (SST) variations (Chu et al., 2014), and variations in sea-ice extent in the Okhotsk Sea (Stebich et al., 2015).

The Northern Hemisphere ice sheets retreated continuously between 12,000–8000 cal yr BP (Fig. 7f) when EASM precipitation gradually increased, as shown by several records from northern China (Xu et al., 2016), including the precipitation record from Tianchi Crater Lake. The clearly synchronous changes in ice volume and EASM precipitation support the significant influence of Northern Hemisphere ice sheets on EASM strength via shifts in the westerlies (Chen et al., 2015) or changing sea level (Li et al., 2014; Sun et al., 2017). In a previous study on reconstructing moisture levels using aeolian deposits and vegetation in the dry lands of northern China, Li et al. (2014) proposed that ice volume-controlled sea-level rise may have shortened the moisture transport distance from the ocean to the continental interior, thus causing the monsoon rainfall belt to migrate northwards. However, the continuous increase in monsoon precipitation after ~8000 cal yr BP is inconsistent with the relative stability of the Northern Hemisphere ice sheets. Moreover, the shrinkage of these ice sheets in the early to mid-Holocene occurred mainly in North America (Peltier, 2004; Törnqvist and Hijma, 2012), which has been suggested to have had little influence on EASM strength (Sundaram et al., 2012). However, additional numerical simulations are needed, because analysis of instrumental data records indicates that climate variations around North America do significantly impact EASM strength (Lu et al., 2006).

The coupled Pacific Ocean–Atmosphere System, which directly transports moisture from the tropical Pacific to the Asian interior and regulates the position of the subtropical monsoon stationary front (Jiang et al., 2012; Chu et al., 2014), is considered a key factor influencing rainfall distribution in the EAM region (Ding and Chan, 2005; Stebich et al., 2015). From a comparison of *n*-alkane and compound-specific carbon isotope records from Xiaolongwan Lake in northeastern China with an SST record from the southern margin of the Okhotsk High, Chu et al. (2014) revealed that decreasing SSTs in the Okhotsk Sea may have strengthened the Okhotsk High and thereby supplied more moisture to northeastern China during the Holocene. The consistency of the SST and precipitation records from Tianchi Crater Lake during the early to mid-Holocene supports the reality of this forcing mechanism. However, at Tianchi Crater Lake, precipitation decreased during the late Holocene, while there was a decrease in the Okhotsk SST record (Fig. 7), and this divergence may be attributed to other factors.

In addition to temperature variations, the Okhotsk Sea ice extent is considered a major regulator of EASM rainfall in northern China (Harada et al., 2014). There is a strong similarity between the quantitative rainfall record from Sihailongwan Lake and the relative abundance of sea-ice-related diatoms from the western Okhotsk Sea, with both records exhibiting an early to mid-Holocene increase with a maximum at ~4000 cal yr BP (Stebich et al., 2015). This linkage is supported by the precipitation record from Tianchi Crater Lake (Fig. 5). However, in view of the complex spatiotemporal variability of marine records (Harada et al., 2014), more precise dating and more robust data interpretation are still needed (Stebich et al., 2015).

Modern instrumental evidence indicates that tropical climate features such as the El Niño–Southern Oscillation (ENSO) are closely connected with the EASM. When an ENSO event occurs, a negative anomaly may appear in the western tropical Pacific Ocean and thus convective activity may be strong around East Asia (Huang and Wu, 1989; Thompson et al., 2017). The west-east thermal gradient in the equatorial Pacific Ocean, serving as a proxy for ENSO variations, is strongly coherent with the EASM record from Gonghai Lake (Chen et al., 2015). Paleo-reconstruction and simulation of ENSO both indicate that El Niño events increased in frequency during the late Holocene, favoring a weak EASM (Chen et al., 2015) and confirming the plausibility of an ENSO influence on variations in EASM precipitation. Nevertheless, peaks in precipitation in northeastern China seem to have occurred later than those at Gonghai Lake in northern China (Chen et al., 2015). The relationship between ENSO-like oscillations and precipitation in northeastern China is thus different from that in northern China and needs further study.

It is clear from the results of this and other studies that rainfall in the EASM region is affected by a complex range of factors and there is no consensus regarding the cause of the delayed onset of the HSMM in northeastern China; it is possible that no single factor was principally responsible. Spatial differences in the timing of the onset of the HSMM, especially those revealed by pollen records (Zhou et al., 2016), clearly need further study to identify the forcing mechanisms. Numerical climate modelling, which can integrate the effects of many factors, may be a useful approach for resolving the issue.

CONCLUSIONS

Changes in vegetation, precipitation, and temperature in northeastern China during the Holocene were reconstructed from the pollen spectra of a sediment core from Tianchi Crater Lake. The fossil pollen data reveal a vegetation transition in the study area from sparse forest steppe to typical forest steppe at ~6500 cal yr BP. The reconstructed precipitation record also features increasing precipitation during the early to mid-Holocene and yields a peak at ~5500–3100 cal yr BP. The trend of reconstructed precipitation is roughly consistent with other pollen-based reconstructions from

northeastern China, with slight differences between the onset times. However, the temperature record exhibits a divergent pattern with a marked rise since the early Holocene and a decrease after ~8000 cal yr BP. Plausible forcing mechanisms for precipitation changes in northeastern China include summer insolation, Northern Hemisphere ice volume, the east-west SST gradient in the tropical Pacific Ocean, and SST and sea-ice changes in the Okhotsk Sea. However, no single factor appears to fully explain the delayed occurrence of the HSMM in northeastern China, indicating the complexity of the forcing of regional rainfall in the EAM region. Further studies, such as simulations and the use of robust proxies, are needed to improve our understanding of the spatiotemporal pattern of the HSMM in the EAM region.

ACKNOWLEDGMENTS

REFERENCES

An, Z., Porter, S.C., Kutzbach, J.E., Wu, X., Wang, S., Liu, X., Li, X., Zhou, W., 2000. Asynchronous Holocene optimum of the East Asian monsoon. *Quaternary Science Reviews* 19, 743–762.

Cai, Y., Tan, L., Cheng, H., An, Z., Edwards, R.L., Kelly, M.J., Kong, X., Wang, X., 2010. The variation of summer monsoon precipitation in central China since the last deglaciation. *Earth and Planetary Science Letters* 291, 21–31.

Caley, T., Roche, D.M., Renssen, H., 2014. Orbital Asian summer monsoon dynamics revealed using an isotope-enabled global climate model. *Nature communications* 5, 6371.

Chen, F., Yu, Z., Yang, M., Ito, E., Wang, S., Madsen, D.B., Huang, X., *et al.*, 2008. Holocene moisture evolution in arid central Asia and its out-of-phase relationship with Asian monsoon history. *Quaternary Science Reviews* 27, 351–364.

Chen, F., Xu, Q., Chen, J., Birks, H., John, B., Liu, J., Zhang, S., Jin, L., *et al.*, 2015. East Asian summer monsoon precipitation variability since the last deglaciation. *Scientific Reports* 5, 11186.

Chen, J., Rao, Z., Liu, J., Huang, W., Feng, S., Dong, G., Hu, Y., Xu, Q., Chen, F., 2016. On the timing of the East Asian summer monsoon maximum during the Holocene: Does the speleothem oxygen isotope record reflect monsoon rainfall variability? *Science China Earth Sciences* 59, 1–11.

Chen, J., Huang, W., Jin, L., Chen, J., Chen, S., Chen, F., 2018. A climatological northern boundary index for the east Asian summer monsoon and its interannual variability. [In Chinese with English translation.] *Science China Earth Sciences* 61:13–22.

Cheng, H., Edwards, R.L., Broecker, W.S., Denton, G.H., Kong, X., Wang, Y., Zhang, R., Wang, X., 2009. Ice age terminations. *Science* 326, 248–252.

Chu, G., Sun, Q., Xie, M., Lin, Y., Shang, W., Zhu, Q., Shan, Y., *et al.*, 2014. Holocene cyclic climatic variations and the role of the Pacific Ocean as recorded in varved sediments from northeastern China. *Quaternary Science Reviews* 102, 85–95.

Clemens, S.C., Prell, W.L., 2007. The timing of orbital-scale Indian monsoon changes. *Quaternary Science Reviews* 26, 275–278.

Dallmeyer, A., Claussen, M., Wang, Y., Herzschuh, U., 2013. Spatial variability of Holocene changes in the annual precipitation pattern: a model-data synthesis for the Asian monsoon region. *Climate Dynamics* 40, 2919–2936.

Ding, Y., Chan, J.C.L., 2005. The East Asian summer monsoon: an overview. *Meteorology and Atmospheric Physics* 89, 117–142.

Dykoski, C.A., Edwards, R.L., Cheng, H., Yuan, D., Cai, Y., Zhang, M., Lin, Y., Qing, J., An, Z., Revenaugh, J., 2005. A high-resolution, absolute-dated Holocene and deglacial Asian monsoon record from Dongge Cave, China. *Earth and Planetary Science Letters* 233, 71–86.

Erdtman, G., 1960. The acetolysis method, a revised description. *Svensk Botanisk Tidskrift* 54, 516–564.

Ficken, K.J., Li, B., Swain, D.L., Eglinton, G., 2000. An n-alkane proxy for the sedimentary input of submerged/floating freshwater aquatic macrophytes. *Organic geochemistry* 31, 745–749.

Goldsmith, Y., Broecker, W.S., Xu, H., Polissar, P.J., deMenocal, P.B., Porat, N., Lan, J., Cheng, P., Zhou, W., An, Z., 2017. Northward extent of East Asian monsoon covaries with intensity on orbital and millennial timescales. *Proceedings of the National Academy of Sciences.* http://dx.doi.org/10.1073/pnas.1616708114.

Gong, J., 1997. Tectonic setting, age and type of Wudalianchi volcanoes. *Heilongjiang Geology* 8, 19–28.

Grimm, E.C., 1987. CONISS: A FORTRAN 77 program for stratigraphically constrained cluster analysis by the method of incremental sum of squares. *Computers & Geosciences* 13, 13–35.

Guo, L., Xiong, S., Ding, Z., Jin, G., Wu, J., Ye, W., 2018. Role of the mid-Holocene environmental transition in the decline of late Neolithic cultures in the deserts of NE China. *Quaternary Science Reviews* 190, 98–113.

Harada, N., Katsuki, K., Nakagawa, M., Matsumoto, A., Seki, O., Addison, J.A., Finney, B.P., Sato, M., 2014. Holocene sea surface temperature and sea ice extent in the Okhotsk and Bering Seas. *Progress in Oceanography* 126, 242–253.

Hong, Y., Hong, B., Lin, Q., Shibata, Y., Hirota, M., Zhu, Y., Leng, X., Wang, Y., Wang, H., Yi, L., 2005. Inverse phase oscillations between the East Asian and Indian Ocean summer monsoons during the last 12000 years and paleo-El Niño. *Earth and Planetary Science Letters* 231, 337–346.

Huang, R., Wu, Y., 1989. The influence of ENSO on the summer climate change in China and its mechanism. *Advances in Atmospheric Sciences* 6, 21–32.

Jiang, W., Guo, Z., Sun, X., Wu, H., Chu, G., Yuan, B., Hatté, C., Guiot, J., 2006. Reconstruction of climate and vegetation changes of Lake Bayanchagan (Inner Mongolia): Holocene variability of the East Asian monsoon. *Quaternary Research* 65, 411–420.

Jiang, W., Guiot, J., Chu, G., Wu, H., Yuan, B., Hatté, C., Guo, Z., 2010. An improved methodology of the modern analogue technique for palaeoclimate reconstruction in arid and semi-arid regions. *Boreas* 39, 145–153.

Jiang, X., He, Y., Shen, C., Kong, X., Li, Z., Chang, Y., 2012. Stalagmite-inferred Holocene precipitation in northern Guizhou Province, China, and asynchronous termination of the Climatic Optimum in the Asian monsoon territory. *Chinese Science Bulletin* 57, 795–801.

Jin, L., Schneider, B., Park, W., Latif, M., Khon, V., Zhang, X., 2014. The spatial-temporal patterns of Asian summer monsoon precipitation in response to Holocene insolation change: A model-data synthesis. *Quaternary Science Reviews* 85, 47–62.

Koutavas, A., Joanides, S., 2012. El Niño–Southern Oscillation extrema in the Holocene and Last Glacial Maximum. *Paleoceanography* 27, PA4208. http://dx.doi.org/10.1029/2012PA002378.

Laskar, J., Robutel, P., Joutel, F., Gastineau, M., Correia, A.C.M., Levrard, B., 2004. A long-term numerical solution for the insolation quantities of the Earth. *Astronomy & Astrophysics* 428, 261–285.

Li, B., 2016. Chinese cultural relics atlas: Helongjiang fascicle. [In Chinese with English translation.] *Northern Cultural Relics* 3: 90–90.

Li, Q., Wu, H., Yu, Y., Sun, A., Marković, S.B., Guo, Z., 2014. Reconstructed moisture evolution of the deserts in northern China since the Last Glacial Maximum and its implications for the East Asian Summer Monsoon. *Global and Planetary Change* 121, 101–112.

Liu, J., 1987. Study on geochronology of the Cenozoic volcanic rocks in Northeast China. *Acta Petrologica Sinica* 4, 21–31.

Liu, J., Chen, S., Chen, J., Zhang, Z., Chen, F., 2017. Chinese cave δ^{18}O records do not represent northern East Asian summer monsoon rainfall. *Proceedings of the National Academy of Sciences* 114, E2987–E2988.

Liu, X., Liu, Z., Kutzbach, J.E., Clemens, S.C., Prell, W.L., 2006. Hemispheric insolation forcing of the Indian Ocean and Asian monsoon: local versus remote impacts. *Journal of Climate* 19, 6195–6208.

Liu, Z., Zhang, K., Sun, Y., Liu, W., Liu, Y., Quan, C., 2014. Cenozoic environmental changes in the northern Qaidam Basin inferred from n-alkane records. *Acta Geologica Sinica* (*English Edition*) 88, 1547–1555.

Lu, R., Dong, B., Ding, H., 2006. Impact of the Atlantic Multidecadal Oscillation on the Asian summer monsoon. *Geophysical Research Letters.* http://dx.doi.org/10.1029/2006GL027655.

Mann, M.E., Zhang, Z., Hughes, M.K., Bradley, R.S., Miller, S.K., Rutherford, S., Ni, F., 2008. Proxy-based reconstructions of hemispheric and global surface temperature variations over the past two millennia. *Proceedings of the National Academy of Sciences* 105, 13252–13257.

Marcott, S.A., Shakun, J.D., Clark, P.U., Mix, A.C., 2013. A reconstruction of regional and global temperature for the past 11,300 years. *Science* 339, 1198–1201.

Max, L., Riethdorf, J.R., Tiedemann, R., Smirnova, M., Lembke-Jene, L., Fahl, K., Nürnberg, D., Matul, A., Mollenhauer, G., 2012. Sea surface temperature variability and sea-ice extent in the subarctic northwest Pacific during the past 15,000 years. *Paleoceanography.* http://dx.doi.org/10.1029/2012PA002292.

Members of China Quaternary Pollen Data Base, 2000. Pollen-based biome reconstruction at middle Holocene (6 ka BP) and last Glacial Maximum (18 ka BP) in China. [In Chinese with English translation.] *Acta Botanica Sinica* 42, 1201–1209.

Members of China Quaternary Pollen Data Base, 2001. Simulation of China biome reconstruction based on pollen data from Surface Sediment Samples. [In Chinese with English translation.] *Acta Botanica Sinica* 43, 201–209.

Moore, P.D., Webb, J.A., 1978. *Illustrated Guide to Pollen Analysis*. Hodder and Stoughton, London.

Nie, J., Song, Y., King, J.W., Zhang, R., Fang, X., 2013. Six million years of magnetic grain-size records reveal that temperature and

precipitation were decoupled on the Chinese Loess Plateau during ~4.5–2.6 Ma. *Quaternary Research* 79, 465–470.

Peck, R.M., 1974. A comparison of four absolute pollen preparation techniques. *New Phytologist* 73, 567–587.

Peltier, W.R., 2004. Global glacial isostasy and the surface of the ice-age Earth: The ICE-5G (VM2) model and GRACE. *Annual Review of Earth and Planetary Sciences* 32, 111–149.

Peng, Y., Xiao, J., Nakamura, T., Liu, B., Inouchi, Y., 2005. Holocene East Asian monsoonal precipitation pattern revealed by grain-size distribution of core sediments of Daihai Lake in Inner Mongolia of north-central China. *Earth and Planetary Science Letters* 233, 467–479.

Peterse, F., Prins, M.A., Beets, C.J., Troelstra, S.R., Zheng, H., Gu, Z., Schouten, S., Sinninghe Damsté, J.S., 2011. Decoupled warming and monsoon precipitation in East Asia over the last deglaciation. *Earth and Planetary Science Letters* 301, 256–264.

Peyron, O., Guiot, J., Cheddadi, R., Tarasov, P., Reille, M., de Beaulieu, J.L., Bottema, S., Andrieu, V., 1998. Climatic reconstruction in Europe for 18,000 yr BP from pollen data. *Quaternary Research* 49, 183–196.

Prentice, I., Guiot, J., Huntley, B., Jolly, D., Cheddadi, R., 1996. Reconstructing biomes from palaeoecological data: A general method and its application to European pollen data at 0 and 6 ka. *Climate Dynamics* 12, 185–194.

Ran, M., Feng, Z., 2013. Holocene moisture variations across China and driving mechanisms: A synthesis of climatic records. *Quaternary International* 313, 179–193.

Rao, Z., Jia, G., Li, Y., Chen, J., Xu, Q., Chen, F., 2016. Asynchronous evolution of the isotopic composition and amount of precipitation in north China during the Holocene revealed by a record of compound-specific carbon and hydrogen isotopes of long-chain n-alkanes from an alpine lake. *Earth and Planetary Science Letters* 446, 68–76.

Reimer, P.J., Bard, E., Bayliss, A., Beck, J.W., Blackwell, P.G., Ramsey, C.B., Buck, *et al.*, 2013. IntCal13 and Marine13 radiocarbon age calibration curves 0–50,000 years cal BP. *Radiocarbon* 55, 1869–1887.

Ren, G., Zhang, L., 1998. A preliminary mapped summary of Holocene pollen data for northeast China. *Quaternary Science Reviews* 17, 669–688.

Shen, H., Wang, X., Dong, L., 2011. Characteristics of main vegetation in Wudalianchi scenic spot of Heilongjiang province. [In Chinese with English translation.] *Northern Horticulture* 1, 108-111.

Stebich, M., Rehfeld, K., Schlütz, F., Tarasov, P.E., Liu, J., Mingram, J., 2015. Holocene vegetation and climate dynamics of NE China based on the pollen record from Sihailongwan Maar Lake. *Quaternary Science Reviews* 124, 275–289.

Sun, A., Feng, Z., 2013. Holocene climatic reconstructions from the fossil pollen record at Qigai Nuur in the southern Mongolian Plateau. *The Holocene* 23, 1391–1402.

Sun, A., Guo, Z., Wu, H., Li, Q., Yu, Y., Luo, Y., Jiang, W., Li, X., 2017. Reconstruction of the vegetation distribution of different topographic units of the Chinese Loess Plateau during the Holocene. *Quaternary Science Reviews* 173, 236–247.

Sun, Y.Y., Zhang, K.X., Liu, J., He, Y.X., Song, B.W., Liu, W.G., Liu, Z., 2012. Long chain alkenones preserved in Miocene lake sediments. *Organic Geochemistry* 50, 19–25.

Sundaram, S., Yin, Q.Z., Berger, A., Muri, H., 2012. Impact of ice sheet induced North Atlantic oscillation on East Asian summer monsoon during an interglacial 500,000 years ago. *Climate Dynamics* 39, 1093–1105.

Tarasov, P., Jin, G., Wagner, M., 2006. Mid-Holocene environmental and human dynamics in northeastern China reconstructed from pollen and archaeological data. *Palaeogeography, Palaeoclimatology, Palaeoecology* 241, 284–300.

Thompson, D.M., Conroy, J.L., Collins, A., Hlohowskyj, S.R., Overpeck, J.T., Riedinger-Whitmore, M., Cole, J.E., *et al.*, 2017. Tropical Pacific climate variability over the last 6000 years as recorded in Bainbridge Crater Lake, Galápagos. *Paleoceanography* 32, 903–922.

Törnqvist, T.E., Hijma, M.P., 2012. Links between early Holocene ice-sheet decay, sea-level rise and abrupt climate change. *Nature Geoscience* 5, 601–606.

Wang, Y., Cheng, H., Edwards, R.L., He, Y., Kong, X., An, Z., Wu, J., Kelly, M.J., Dykoski, C.A., Li, X., 2005. The Holocene Asian monsoon: Links to solar changes and North Atlantic climate. *Science* 308, 854–857.

Wang, Y., Cheng, H., Edwards, R.L., Kong, X., Shao, X., Chen, S., Wu, J., Jiang, X., Wang, X., An, Z., 2008. Millennial- and orbital-scale changes in the East Asian monsoon over the past 224,000 years. *Nature* 451, 1090–1093.

Webster, P.J., 2006. The coupled monsoon system. *The Asian Monsoon*, 3–66.

Wen, R., Xiao, J., Chang, Z., Zhai, D., Xu, Q., Li, Y., Itoh, S., 2010. Holocene precipitation and temperature variations in the East Asian monsoonal margin from pollen data from Hulun Lake in northeastern Inner Mongolia, China. *Boreas* 39, 262–272.

Wen, R., Xiao, J., Fan, J., Zhang, S., Yamagata, H., 2017. Pollen evidence for a mid-Holocene East Asian summer monsoon maximum in northern China. *Quaternary Science Reviews* 176, 29–35.

Xia, D., Jia, J., Li, G., Zhao, S., Wei, H., Chen, F., 2014. Out-of-phase evolution between summer and winter East Asian monsoons during the Holocene as recorded by Chinese loess deposits. *Quaternary Research* 81, 500–507.

Xia, Y., 1988. Preliminary study of vegetational development and climatic changes in the Sanjiang Plain in the last 12000 years. [In Chinese with English translation.] *Scientia Geographica Sinica* 8, 240–249.

Xiao, J., Si, B., Zhai, D., Itoh, S., Lomtatidze, Z., 2008. Hydrology of Dali Lake in central-eastern Inner Mongolia and Holocene East Asian monsoon variability. *Journal of Paleolimnology* 40, 519–528.

Xiao, J., Fan, J., Zhai, D., Wen, R., Qin, X., 2015. Testing the model for linking grain-size component to lake level status of modern clastic lakes. *Quaternary International* 355, 34–43.

Xu, Q., Xiao, J., Li, Y., Tian, F., Nakagawa, T., 2010. Pollen-based quantitative reconstruction of Holocene climate changes in the Daihai Lake area, Inner Mongolia, China. *Journal of Climate* 23, 2856–2868.

Xu, Q., Chen, F., Zhang, S., Cao, X., Li, J., Li, Y., Li, M., Chen, J., Liu, J., Wang, Z., 2016. Vegetation succession and East Asian Summer Monsoon Changes since the last deglaciation inferred from high-resolution pollen record in Gonghai Lake, Shanxi Province, China. *The Holocene* 27, 835–846.

Xu, Y., Jaffé, R., 2009. Geochemical record of anthropogenic impacts on Lake Valencia, Venezuela. *Applied Geochemistry* 24, 411–418.

Yu, S., 2013. Quantitative reconstruction of mid- to late-Holocene climate in NE China from peat cellulose stable oxygen and carbon isotope records and mechanistic models. *The Holocene* 23, 1507–1516.

Zhang, J., Tsukamoto, S., Jia, Y., Frechen, M., 2016. Lake level reconstruction of Huangqihai Lake in northern China since MIS 3 based on pulsed optically stimulated luminescence dating. *Journal of Quaternary Science* 31, 225–238.

Zhao, C., 2015. The Vegetation Succession and Response to Climate Change in northern Northeast China for the last 30 ka BP (Ph.D. thesis). University of Chinese Academy of Sciences.

Zhao, Y., Yu, Z., Chen, F., Zhang, J., Yang, B., 2009. Vegetation response to Holocene climate change in monsoon-influenced region of China. *Earth-Science Reviews* 97, 242–256.

Zhou, W., Song, S., Burr, G., Jull, A.J.T., Lu, X., Yu, H., Cheng, P., 2007. Is there a time-transgressive Holocene optimum in the East Asian monsoon area? *Radiocarbon* 49, 865–875.

Zhou, W., Zheng, Y., Meyers, P.A., Jull, A.J.T., Xie, S., 2010. Post-glacial climate-change record in biomarker lipid compositions of the Hani peat sequence, northeastern china. *Earth and Planetary Science Letters* 294, 0–46.

Zhou, X., Sun, L., Zhan, T., Huang, W., Zhou, X., Hao, Q., Wang, Y., *et al*., 2016. Time-transgressive onset of the Holocene Optimum in the East Asian monsoon region. *Earth and Planetary Science Letters* 456, 39–46.